Phase-contrast tomography of sciatic nerves: image quality and experimental parameters

IOP Conf. Series: Journal of Physics: Conf. Series **849** (2017) 012001 doi:10.1088/1742-6596/849/1/012001

Phase-contrast tomography of sciatic nerves: image quality and experimental parameters

M Töpperwien[1,2,a)], M Krenkel[1], T Ruhwedel[3], W Möbius[2,3], A Pacureanu[4], P Cloetens[4] and T Salditt[1,2,b)]

[1] Institut für Röntgenphysik, Friedrich-Hund-Platz 1, 37077 Göttingen, Germany
[2] Center for Nanoscopy and Molecular Physiology of the Brain, Göttingen, Germany
[3] Max-Planck-Institut für Experimentelle Medizin, Hermann-Rein-Str. 3, 37075 Göttingen, Germany
[4] European Synchrotron Radiation Facility, Grenoble, France

E-mail: [a)]mtoeppe@gwdg.de, [b)]tsaldit@gwdg.de

Abstract. We present propagation-based phase-contrast tomography of mouse sciatic nerves stained with osmium, leading to an enhanced contrast in the myelin sheath around the axons, in order to visualize the threedimensional (3D) structure of the nerve. We compare different experimental parameters and show that contrast and resolution are high enough to identify single axons in the nerve, including characteristic functional structures such as Schmidt-Lanterman incisures.

Assessing the three-dimensional structure of myelinated nerves is required in order to fully understand the function of the nerve based on its anatomical features. A standard tool for imaging of nerve tissue is electron microscopy which leads to high resolution reconstructions of the inner structure of the nerve but is limited to small volumes. (Hard) x-ray computed tomography is a promising approach for 3D imaging of relatively large volumes, especially by using the phase shift instead of the absorption of the beam, as this leads to superior contrast in soft tissue. High resolution reconstructions can be achieved via propagation-based phase contrast exploiting the near-field intensity modulations resulting from free space propagation between the object and the detector [1, 2]. By applying suitable phase retrieval algorithms the quantitative phase distribution of the object can be obtained [3]. In a previous study of our group, propagation-based imaging of high-pressure frozen nerves was performed at the ID22NI beamline at the ESRF in Grenoble, yielding high contrast reconstructions of the axons within the nerve and making anatomical features like Schmidt-Lanterman incisures visible in 3D [4]. However, since then the new ESRF upgrade beamline ID16A [5], as well as an upgrade of the GINIX endstation at the P10 beamline at DESY in Hamburg [6] have been commissioned. The scope of this paper is to assess the image quality of the reconstructions obtained at these two setups and to evaluate whether a comparable resolution and contrast can be achieved.
Reconstruction starts with phase retrieval for the individual projections recorded at each angle of a tomographic scan. The phase retrieval schemes applied in this work are based on the contrast transfer function (CTF) which is valid for weak or non-absorbing objects with a slowly varying phase. The theory underlying these reconstruction schemes can be found, e.g., in [7, 8, 9]. Crucial parameters for the reconstruction are the number of propagation distances between the

Table 1. Experimental parameters.

	GINIX overview	GINIX zoom	ID16A
energy [keV]	13.8	13.8	17.05
z_1/z_2 [mm]	140/5187	50/5187	53/337
detector	sCMOS (Hamamatsu)	sCMOS (Hamamatsu)	FReLoN (ESRF)
pixel size/eff. pixel size [nm]	6500/182.8	6500/62.7	845/131.8
# distances/$\frac{\#\text{ projections}}{\text{distance}}$	4/1000	4/1000	4/1995
expos. time [s]	1	1	0.2
CTF $\frac{\delta}{\beta}/\alpha_1/\alpha_2$	6/-/1e-04	10/-/1e-06	-/1e-05/0.01

sample and the detector as well as the choice of the regularization parameters α_1 or $\frac{\delta}{\beta}$ and α_2 which are defined as in [4]. As a final step in data analysis, tomographic reconstruction is carried out using the Matlab implemented *iradon* function with a standard Ram-Lak filter.
The sciatic nerves of two adult mice were prepared freshly and fixed by immersion into 4% formaldehyde, 2.5% glutaraldehyde in 0.1 M phosphate buffer pH 7.3 and 0.5% NaCl. After postfixation in 2% OsO4 in 0.1 M phosphate buffer for 4h at 4 °C and dehydration with ethanol and propylenoxide, the nerves were embedded in EPON, transferred into a Kapton tube and polymerized for 24h. Experiments have been carried out at the ID16A beamline at the ESRF in Grenoble, as well as the GINIX setup at the P10 beamline at DESY in Hamburg. In the case of the ID16A beamline the photons are focussed by a set of Kirkpatrick-Baez (KB) mirrors to a focus size of 26 × 39 nm^2 (FWHM, h×v) whereas in the case of the GINIX setup the beam is prefocussed by a KB system to a size of about 300×300 nm^2 and further shaped by placing a waveguide into the focus, minimizing the focal spot size to approximately 18×18 nm^2 (FWHM) while at the same time increasing the coherence [10]. Due to the cone-beam geometry in both setups, the effective pixel size can be changed by varying the geometrical magnification $M = \frac{z_2}{z_1}$, with z_2 the focus-detector-distance and z_1 the focus-sample-distance. The experimental parameters for each measurement are summarized in Tab. 1.
In Fig. 1 the basic steps of data analysis are illustrated for the example of the high resolution measurement at the P10 beamline. Data analysis starts with the empty-beam corrected

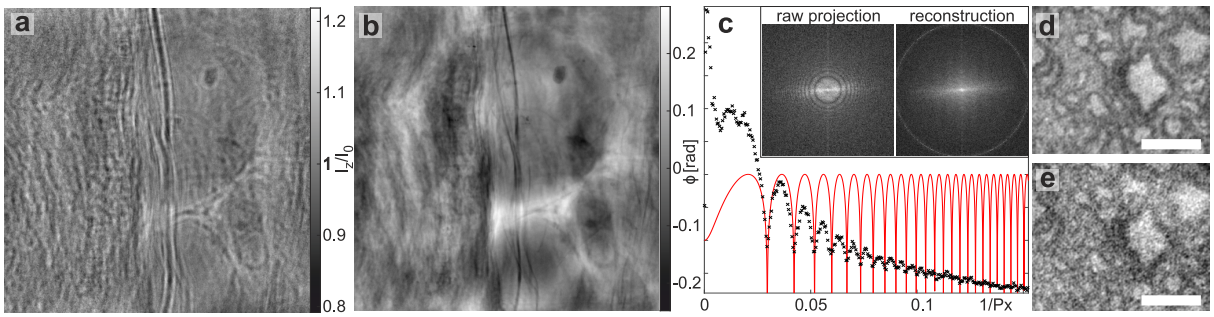

Figure 1. Schematics of the phase-retrieval procedure. (a) Empty-beam corrected projection of the sample. (b) Reconstructed phase of the same projection. (c) Inset: Central part of the power spectral density (PSD) of the projections from (a) and (b). Graph: Logarithmic PSD of the experimental data (black) compared to the theoretical shape according to the CTF (red, for visibility shifted and scaled). (d) Part of an exemplary slice through the volume using 4 distances for phase retrieval. (e) The same slice using only a single distance. Scalebars: 10 μm

projection shown in (a). For each of the individual projections phase retrieval with one of the two CTF approaches has to be performed, leading to the reconstructed phase distribution in (b). Due to the different magnifications at different propagation distances, images have to be rescaled and aligned to the projection with the smallest effective pixel size prior to phase retrieval. When looking at the power spectral density (PSD) of the empty-beam corrected raw projection in (c, left) the typical oscillations predicted by the CTF are visible. However, a comparison with the theory shows that the visibility of the modulations is decreasing, especially for higher spatial frequencies, which can be explained by the violation of the weak object assumption [11]. This leads to the introduction of high-frequency artifacts in the phase reconstruction as can be seen in the corresponding PSF (c, right). As the CTF approach nevertheless provides reasonable results, it is in the following used for reconstruction of the 3D density distribution. One exemplary virtual slice through the volume with several propagation distances taken into account is shown in (d) whereas for the slice in (e) only one propagation distance was used. As can be seen in the insets, a reasonable reconstruction of the general shape of the object is still possible. However, when aiming for highest resolution and contrast the use of several distances is inevitable.

At the GINIX setup two datasets with different magnifications were recorded, one with a pixel size of 182.8 nm, in the following denoted as the 'overview' scan, and one with a pixel size of 62.7 nm, in the following denoted as the 'zoom' dataset. Phase retrieval was performed using the parameters listed in Tab. 1. The results of both scans are visualized in Fig. 2. One virtual transverse slice through the reconstructed volume of the overview scan is shown in (a), revealing the typical structure of the mylin sheath around the individual axons in the nerve. Note that the contrast is decreasing towards the middle of the nerve which can be explained by an unequal penetration of the osmium throughout the whole nerve. The inset shows part of the slice in higher detail as well as the result of the zoom dataset as a comparison, showing the advantage in resolution. In order to get a higher signal-to-noise ratio (SNR) both datasets were filtered with a Gaussian with a 0.7 pixel (overview) and a 2 pixel kernel (zoom), respectively. The resulting SNRs are approximately 7.6 and 4.7 for the outer and inner region in the overview scan and 6.1

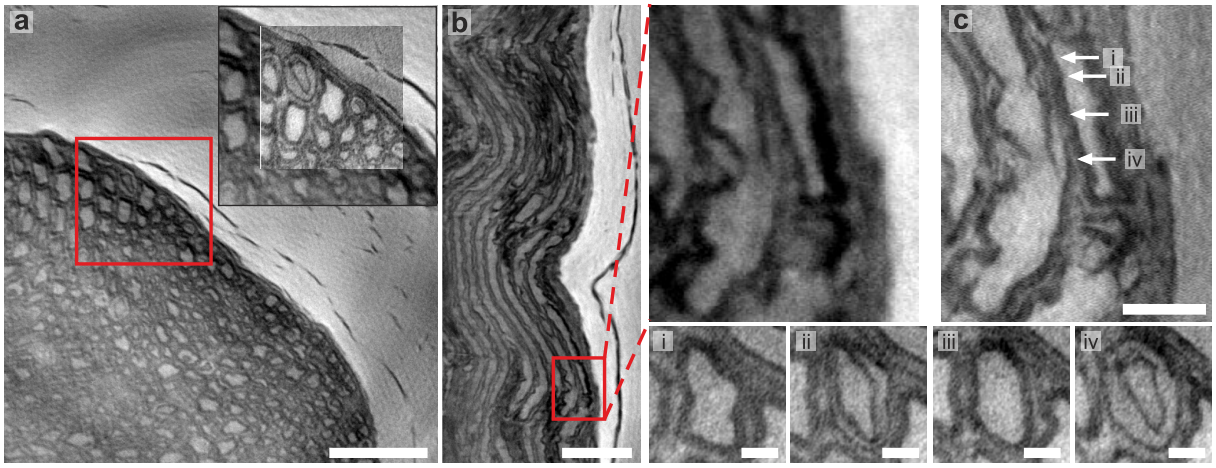

Figure 2. Measurement at the GINIX setup at the P10 beamline. (a) Virtual transverse slice through the reconstructed 3D density distribution of the large overview scan. The inset shows a comparison between the image quality of the overview and the high resolution scan. (b) Virtual longitudinal slice. (c) Same slice for the zoom dataset showing the inset in (b) in higher detail. (i-iv) Parts of transverse slices at the positions indicated by the arrows. Scalebars: (a,b) 50 μm, (c) 10 μm, (i-iv) 5 μm

for the zoom dataset. To estimate the resulting resolution, an error function is fitted to the edge of an object within the reconstructed volume. This gives 465.8 nm and 291.6 nm (FWHM), respectively. The longitudinal slice in (b) reveals the orientation of the axons within the sciatic nerve, showing the typical shevron pattern observed previously [4]. Additionally, anatomical features like the Schmidt-Lanterman incisures, clefts in the myelin sheath around the axons, can be identified in the reconstructed slices, see (c, i-iv).
In Fig. 3 the results of the dataset recorded at the ID16A setup with a pixel size of 131.8 nm are shown. The transverse slice in (a) again reveals the typical shape of the myelin sheath around the axons, though more uniformly stained compared to the nerve in Fig. 2 and at a higher SNR of approximately 9.7 (no filter was applied). The resolution can be estimated as 303.1 nm (FWHM), again by fitting an error function to the edge of an object. The longitudinal slice in (b) shows the course of the axons within the nerve whereas in the inset in (c) as well as the transverse slices at the positions indicated by the arrows the typical Schmidt-Lanterman incisures can again be clearly recognized.
The reconstructions from both experimental setups provide a data quality high enough for identification of the individual axons in the nerve as well as typical anatomical features like the Schmidt-Lanterman incisures. In contrast to the previous study samples were not high pressure frozen but prepared according to standard protocols for electron microscopy, still yielding at least comparable contrast within the tissue.
The next step would still be an automatic rendering of the data including the quantification of the number of axons within the nerve as well as the recognition of anatomical features like Schmidt-Lanterman incisures or nodes of Ranvier and their frequency of occurrence and spatial distribution along the nerve. This will pave the way for biomedical studies aiming for the quantification of structural differences between different phenotypes in relatively large volumes of interest.

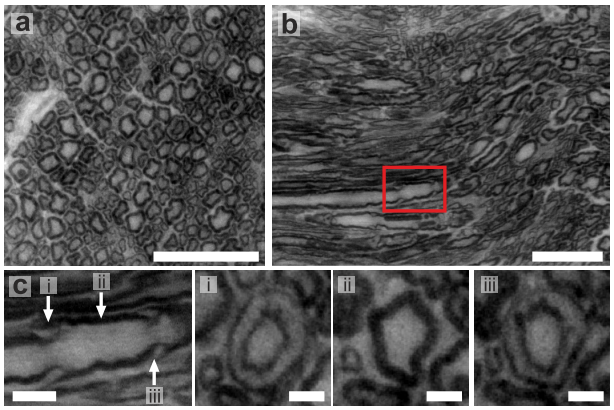

Figure 3. Measurement at ID16A beamline. (a) Virtual transverse slice through the reconstructed 3D density distribution. (b) Virtual longitudinal slice. (c) Inset of the longitudinal slice in (b) showing part of the myelin sheath around the one axon in higher detail. (i-vi) Parts of transverse slices at the positions indicated by the arrows. Scalebars: (a,b) 50 μm, (c) 10 μm, (i-iii) 5 μm

Acknowledgments
We thank Michael Sprung for excellent support during our beamtimes at P10. We particularly thank Matthias Bartels for discussions, and the establishment of methods in a preceeding collaboration on nerve tomography. This work was supported by the Collaborative Research Center 755 *Nanoscale Photonic Imaging* of the German science foundation (DFG).

References
[1] Zanette I, Lang S, Rack A, Dominietto M, Langer M, Pfeiffer F, Weitkamp T and Müller B 2013 *Appl. Phys. Lett.* **103** 244105
[2] Bartels M, Krenkel M, Haber J, Wilke R N and Salditt T 2015 *Phys. Rev. Lett.* **114**(4) 048103

[3] Paganin D M 2006 *Coherent X-Ray Optics* (New York: Oxford University Press)
[4] Bartels M, Krenkel M, Cloetens P, Möbius W and Salditt T 2015 *Journal of structural biology* **192** 561–568
[5] Morawe C, Barrett R, Cloetens P, Lantelme B, Peffen J C and Vivo A 2015 *SPIE Optical Engineering+ Applications* (International Society for Optics and Photonics) pp 958803–958803
[6] Salditt T, Osterhoff M, Krenkel M, Wilke R N, Priebe M, Bartels M, Kalbfleisch S and Sprung M 2015 *J. Synchrotron Rad.* **22** 867–878
[7] Cloetens P, Ludwig W, Baruchel J, Van Dyck D, Van Landuyt J, Guigay J P and Schlenker M a 1999 *Appl. Phys. Lett.* **75** 2912–2914
[8] Zabler S, Cloetens P, Guigay J P, Baruchel J and Schlenker M 2005 *Rev. Sci. Instrum.* **76** 073705
[9] Turner L, Dhal B, Hayes J, Mancuso A, Nugent K, Paterson D, Scholten R, Tran C and Peele A 2004 *Opt. Express* **12** 2960–2965
[10] Krüger S P, Neubauer H, Bartels M, Kalbfleisch S, Giewekemeyer K, Wilbrandt P J, Sprung M and Salditt T 2012 *J. Synchrotron Rad.* **19** 227–236
[11] Moosmann J, Hofmann R and Baumbach T 2011 *Optics express* **19** 12066–12073